



# The contribution of glacial isostatic adjustment to relative sea-level rise and land subsidence along the Atlantic coast of Europe

Geoffrey Chapman <sup>a</sup>, Glenn A. Milne <sup>a,\*</sup> , Soran Parang <sup>a</sup> , Parviz Ajourlou <sup>a</sup> , Ryan Love <sup>a</sup>, Adélaïde Gunn <sup>a</sup>, Lev Tarasov <sup>b</sup>

<sup>a</sup> Department of Earth and Environmental Sciences, University of Ottawa, Ottawa, Canada

<sup>b</sup> Department of Physics and Physical Oceanography, Memorial University, St John's, Newfoundland, Canada

## ARTICLE INFO

Handling Editor: Qiuzhen Yin

**Keywords:**

Sea level changes  
Glacial isostatic adjustment  
Vertical land motion  
Forward modelling  
Atlantic coast of Europe  
Tide gauge

## ABSTRACT

We quantify the contribution of glacial isostatic adjustment (GIA) to land subsidence and sea-level rise along the Atlantic coast of Europe. Using both geologic reconstructions of relative sea-level (RSL) change and geodetic determinations of vertical land motion, we assess GIA model accuracy and determine model parametric uncertainty. Seven ice history models and 440 spherically symmetric Earth viscosity models were used to explore the model parameter space. Our results indicate that the inferred earth model parameters are highly dependent on the barystatic component of the adopted ice sheet model. On the other hand, the modelled RSL output is relatively insensitive to variations in the ice thickness distribution of the Eurasian component of the ice history model. Of the two global ice models considered (ANU and ICE-6G) our results demonstrate the barystatic component of the ANU model to be more accurate. Model uncertainty was determined using data-model misfit values and a Bayesian approach to define a subset of parameter sets ( $1\sigma$  confidence). When considering the model uncertainty, 95 % of the Holocene RSL observations and 93 % of the present-day vertical land motion rates can be explained at this confidence level. Our results support previous work in showing that GIA-related subsidence along the Atlantic coast of Europe is dominated by ice-loading (peripheral bulge) effects and that ocean loading is also important in some areas, such as northwestern France. Using our subset of best-fitting parameter sets, we performed a sea-level budget analysis for the period 1957 to 1997 using data from 10 tide gauges in our study region and find that the sterodynamic signal is the largest contributor at most of the considered tide gauge sites, followed by contributions from GIA and glaciers. The GIA signal dominates the modelled uncertainty at all sites. Of the 10 tide gauge stations considered, the budget is closed at six (to within  $2\sigma$  uncertainty). The largest residual was found for station Dieppe in northern France, with an unexplained signal of  $3.8 \pm 0.6$  mm/yr, which appears to be related to localized subsidence at the tide gauge site.

## 1. Introduction

Anthropogenic climate change continues to produce sea-level rise through global climate warming at an accelerating rate (Fox-Kemper et al., 2021). It is thus important to better understand and quantify contributions to contemporary and future sea-level change. One route to this goal involves considering records of ice sheet and sea-level changes since the Last Glacial Maximum (LGM; 26.5 to 19 ka; Clark et al., 2009) with an aim to better understand the deglaciation process and its effects on sea level. Not only does this route provide a better understanding of the most recent deglaciation event and the underlying processes, but this major climate transition continues to impact changes in sea level both

globally and locally through the process of glacial isostatic adjustment (GIA).

GIA is the response of the solid Earth to past surface loading associated with ice-ocean mass transfer (e.g., Spada, 2017; Whitehouse, 2018) and is known to be more significant in regions proximal to the late Quaternary ice sheets, such as in North America, Northern Europe, and Fennoscandia. In most regions once covered by ice sheets, GIA results in contemporary upward vertical land motion (VLM), while in areas near or beyond the LGM ice margins, GIA often results in downward VLM (e.g., Peltier, 1996; Peltier, 2004). This latter area is referred to as the peripheral bulge, where subsidence is observed during most of the deglaciation and in contemporary times (e.g., Muhs et al., 2012; Goslin

\* Corresponding author.

E-mail address: [gamilne@uottawa.ca](mailto:gamilne@uottawa.ca) (G.A. Milne).

et al., 2015). Local rates of contemporary sea-level change can vary considerably from the global average (e.g., Slangen et al., 2012; Fox-Kemper et al., 2021) due to various factors including the GIA process (Karegar et al., 2016).

Quantifying the GIA contribution to current and future sea-level change is important, particularly in peripheral bulge regions where it generally enhances the other component signals. This task relies on the availability of paleo relative sea level (RSL) datasets which often provide the best constraints on GIA model parameters. In the past decade there has been a focused community effort to produce regional RSL databases in a standardized format (Khan et al., 2019), which has led to a growing number of high-quality databases being made available to constrain GIA models (e.g., Love et al., 2016; Yousefi et al., 2018; Li et al., 2020). A recently published dataset for the Atlantic coast of Europe (García-Artola et al., 2018), which is part of this community effort (known as the HOlocene relative SEA level (HOLSEA) initiative), motivated and enabled the GIA modelling analysis presented in this paper.

Previous work has explored the effects of GIA on sea-level change in North America on both eastern (Davis and Mitrovica, 1996; Wake et al., 2006; Engelhart et al., 2009; Roy and Peltier, 2015; Love et al., 2016; Williams et al., 2024) and western coasts (James et al., 2009; Yousefi et al., 2018). For example, Love et al. (2016) estimated an RSL rise of 3–18 cm between 2000 and 2100 CE (based on optimal parameter values) from St John's, Newfoundland, Canada, to Galveston, Texas, USA. Along the central western coast of North America, Yousefi et al. (2018) constrained the GIA contribution (over the period 2010–2100 CE) to range from −2.2 cm in Seattle, Washington, USA to a rise of 14.44 cm in Crescent City, California, USA. Thus, peripheral bulge subsidence is a significant contributor to RSL rise on the Atlantic and Pacific coasts of North America.

On the eastern side of the North Atlantic, there have been significantly fewer studies focusing on constraining the contribution of GIA to regional-scale land subsidence and RSL rise. The most extensive modeling studies have focused on near-field regions such as Fennoscandia (e.g., Lambeck et al., 1998) and the British Isles (e.g., Bradley et al., 2023). There have been isolated studies that have sought to quantify the processes contributing to land subsidence, including GIA, at selected locations (e.g., Gehrels et al., 2011; Goslin et al., 2015; Li et al., 2024). On regional scales, Holocene RSL rise has been studied in the Mediterranean Sea (e.g., Lambeck and Bard, 2000; Vacchi et al., 2016) and the Atlantic coast of France, Spain, and Portugal (Leorri et al., 2012; García-Artola et al., 2018). However, these studies focused on the RSL reconstructions rather than seeking to develop an improved estimate of GIA model parameters and quantify the contribution of this process to land subsidence and RSL rise.

Observations of VLM using the Global Navigation Satellite System (GNSS) have also been used to constrain and quantify the contribution of GIA to land subsidence in peripheral bulge regions (e.g., Park et al., 2002; Sella et al., 2007). Recent analyses have considered both VLM and geological RSL observations to determine if the more recent GNSS-determined rate is different to the background millennial trend that is dominated by GIA in tectonically stable areas. This enables identification of locations where non-GIA processes are active – for example, signals associated with recent hydrological changes or glacier mass loss (e.g., Karegar et al., 2016; Yousefi et al., 2020) – and, therefore, a better understanding and quantification of the sea-level drivers.

Our primary aim is to quantify, with uncertainty, the GIA contribution to land subsidence and RSL rise along the Atlantic Coast of Europe. We extend past work (Leorri et al., 2012; García-Artola et al., 2018) by considering a much larger GIA (earth and ice) model parameter set and by including a VLM dataset developed for the purpose of constraining GIA models (Schumacher et al., 2018). Our results can be used to interpret geodetic records of sea level change and VLM, or sum component signals to project future sea level change (Slangen et al., 2012). As an illustration of such applications, we include a sea-level

budget analysis to determine the relative importance of GIA for understanding late 20th century RSL changes in the study region.

## 2. Methods

### 2.1. RSL data

Holocene sea-level data are taken from a recently published RSL database (García-Artola et al., 2018). The data are partitioned into 13 sites (García-Artola et al., 2018, Fig. 1) and constrain Holocene RSL changes from northern France to southern Portugal. These site locations were preserved for individual site analysis, while also being grouped into 4 regions to investigate the possibility of lateral Earth structure variations affecting RSL along this coastline. These four regions are the Northern French coast (sites 1–4), western French coast (sites 5–7), and north and west Iberian Peninsula coasts (sites 8–10 and 11–13 respectively). The dataset is comprised of 340 data points, 214 of these are sea level index points (SLIPs) and 126 limiting data points. SLIPs indicate a specific range in space and time dictated by uncertainty in which sea

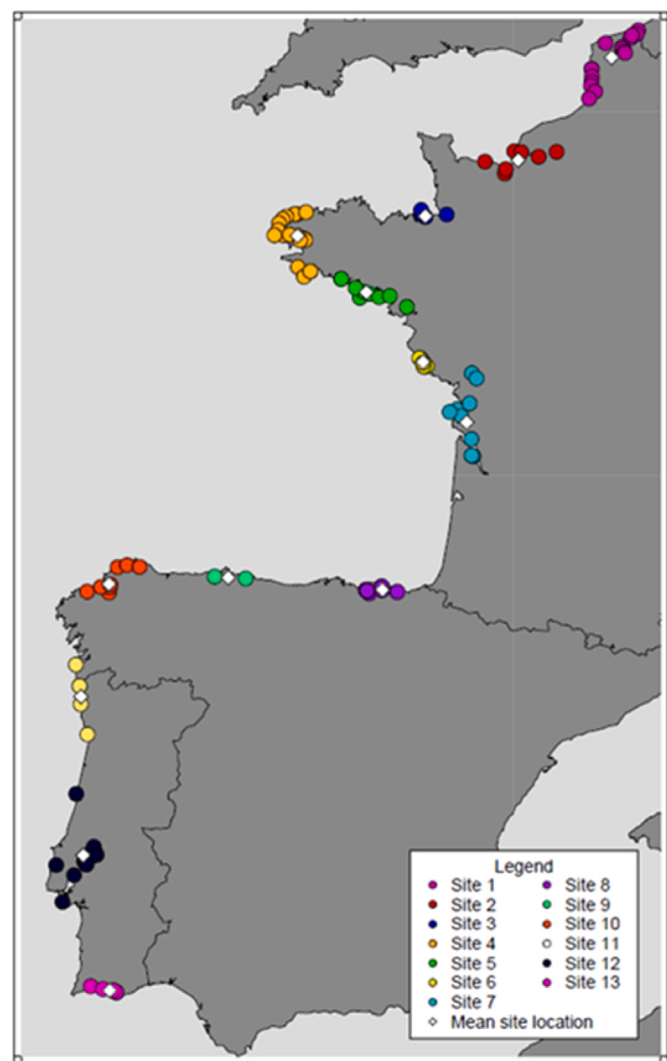


**Fig. 1.** Map showing the spatial distribution of RSL data points across the study area. Mean site locations are denoted by white diamonds, whereas locations of individual datapoints (corresponding to SLIPs and limiting data points) are denoted by coloured circles with a different colour corresponding to each of the 13 site locations. Solid black lines denote national borders. (For interpretation of the references to colour in this figure legend, the reader is referred to the Web version of this article.)

level was located, while limiting data points, divided into marine limiting (ML) and terrestrial limiting (TL), indicate that sea level had to exist above (ML) or below (TL) them (considering height and time uncertainty) (e.g., Khan et al., 2019; Shennan et al., 2015).

Fig. 2 displays all data points on a single RSL-time plot. While this is inaccurate due to the considerable spatial variability in RSL across this region, we include it to provide a concise visual indication of the regional RSL signal. A more accurate presentation, with data partitioned into the 13 sites can be found in García-Artola et al. (2018), and in Section 3.1 below. It is important to note that some revisions were made to the original data set; specifically, the ages were re-calibrated using the most recent calibration curves made available via IntCal20 (Reimer et al., 2020) and Marine20 (Heaton et al., 2020). Some limiting data points were removed (25 ML and 4 TL) as they were redundant in terms of constraining RSL (e.g., ML data plotting beneath other ML data spanning the same time interval). The greatest number of redundant limiting data were identified at site 8 and so, to illustrate an example of this data cleaning process, data are shown for this site before and after removal of the redundant limiting points (Fig. S1).

The removal of redundant limiting data points was undertaken as their presence affects the data-model comparison via the misfit criterion (Eqn. (2); Section 2.4). Specifically, the misfit criteria are normalized by the number of data points included, and thus redundant limiting data points bias the calculated misfit to a lower value. Removal of these data thus leads to more accurate model parameter and uncertainty estimation.

In addition to removing some of the limiting data, a small number of

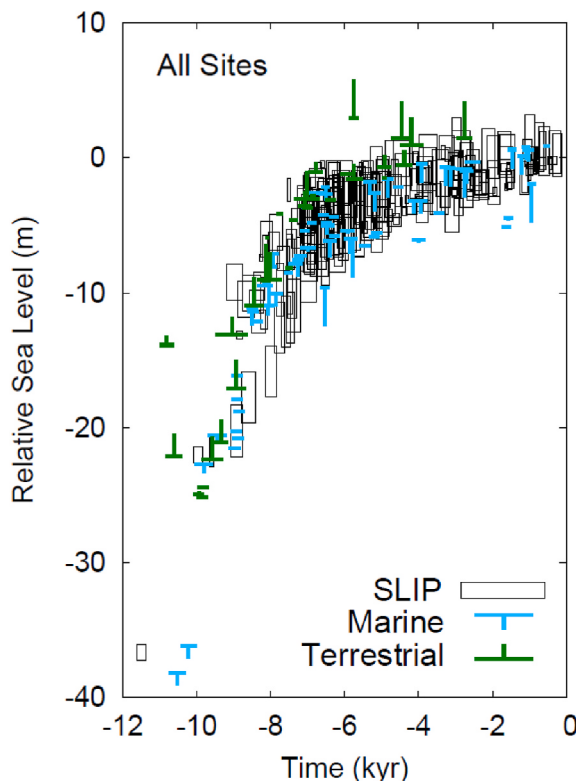


**Fig. 2.** Reconstructed RSL for data locations shown in Fig. 1. Original dataset is from García-Artola et al. (2018), with ages recalibrated and some limiting data points removed (see text for details). The symbols are scaled to represent  $1\sigma$  uncertainty ranges in time and RSL. Limiting data are plotted using upright or inverted 'T-shaped' symbols for marine and terrestrial points (blue and green respectively) with the location of the horizontal line indicating the mid-point of the height measurement and the width of this line representing the  $\pm 1\sigma$  time uncertainty range (Khan et al., 2015). (For interpretation of the references to colour in this figure legend, the reader is referred to the Web version of this article.)

SLIPs were also removed prior to the modelling analysis. Site 8 includes 12 SLIPs in the late Holocene which appear anomalously low when compared to ML points during the mid-Holocene (~7 ka) at this site. Furthermore, García-Artola et al. (2018) remark (p. 189) that these saltmarsh SLIPs are likely affected by sediment compaction due to land drainage for agricultural purposes. A more recent study (Li et al., 2024) argues that non-GIA processes are responsible for the high rates of late Holocene RSL rise indicated by the late Holocene SLIPs at site 8. We have thus elected to omit all SLIP data points from site 8. We also did not consider the three oldest SLIPs from site 9 as they are not compatible with ML points at ~2 m elevation during the mid-Holocene at this site. Although these SLIPs were not considered in our data-model misfit calculations and thus model parameter estimation, they are included in the relevant figures (using dashed outlines) for completeness. As a final comment, we did compute data-model misfits with and without the suspect SLIPs at sites 8 & 9 and found that the primary results of this study are not affected.

Following García-Artola et al. (2018), the regional characteristics of reconstructed RSL along the Atlantic coast of Europe can be summarized as follows. Early Holocene constraints begin around ~36 m below present sea level at 11.7 ka and show a rapid rise in RSL at a rate of approximately 6–6.2 m/kyr until ~6 ka when the rate significantly decreases (Fig. 2). The regional sea-level rise continues at a much slower rate (~1 m/kyr) through the mid-to-late Holocene. This temporal variation reflects a general slowdown in global ice sheet melting in the mid-Holocene (Lambeck et al., 2014). The slower but significant rate of RSL rise during the late Holocene (~6 ka to present) is characteristic of peripheral bulge regions, where GIA-associated land subsidence is a significant factor (Clark et al., 1978; Engelhart et al., 2009; Leorri et al., 2012).

## 2.2. GNSS and tide gauge data

Global Navigation Satellite System (GNSS) data are taken from the global VLM data set presented by Schumacher et al. (2018) in which signals not associated with GIA were removed or diminished. Specifically: (1) VLM rates were estimated for the period 2005 to 2015 considering stations with at least 4 years of continuous data collection such that the calculated rates are not strongly influenced by shorter time scale processes, (2) stations with rates that lie outside a 3-sigma range defined using 13 global GIA forward model solutions were removed, and (3) a model estimate of contemporary elastic signals associated with mass changes in ice sheets and glaciers as well as short-term polar motion were removed. Hydrological and atmospheric loading VLM signals were not removed due to their large uncertainty. Further details can be found in Schumacher et al. (2018).

For geographic consistency with the RSL data, we considered only a subset of the Schumacher et al. (2018) data set from our study region. Specifically, only stations within 150 km of the Atlantic coastline. Other distances were considered (e.g., 50 km, 250 km) but 150 km was adopted as it provides a good balance between coastal proximity and sufficient density of data points along the shoreline (Fig. 3). As expected, the VLM rates for this data set reflect peripheral bulge subsidence.

We applied the GIA model constraints obtained in this work to perform a sea-level budget analysis (Section 3.2.2). We used data from the Permanent Service for Mean Sea Level (<https://psmsl.org/data/>) to determine the rates of RSL change over the 40-year period 1957–1997. Only ten stations provided relatively continuous RSL time series over this period in our study area (Fig. 3).

## 2.3. GIA model

The GIA model used to calculate changes in sea level and VLM assumes a spherically symmetric, compressible Earth with a Maxwell rheology (Peltier, 1974). The depth-dependent viscosity structure is parameterised into three layers, with the lithosphere as a highly viscous

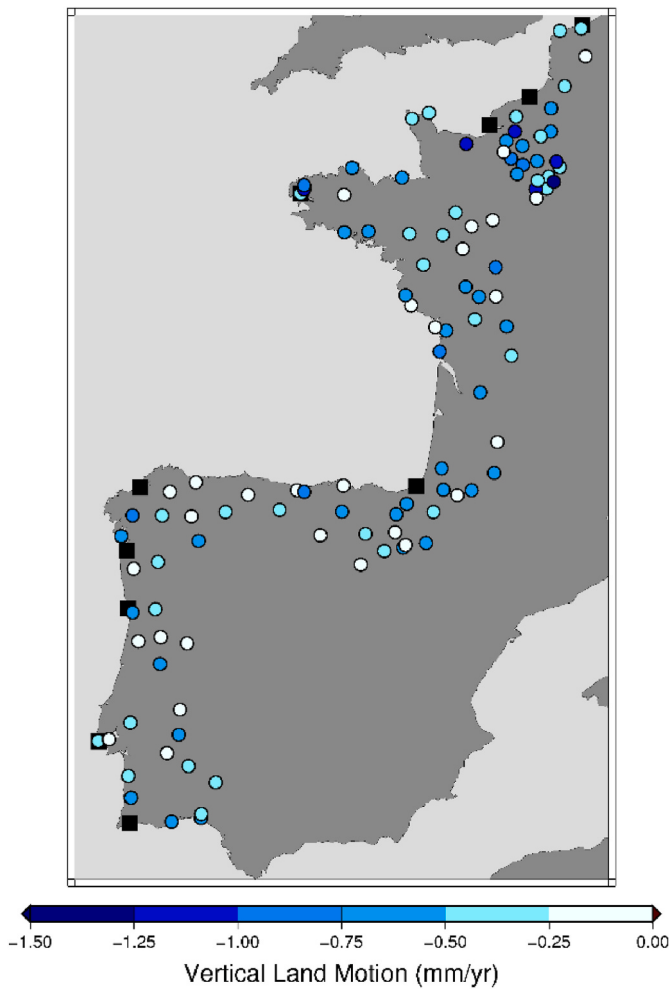


**Fig. 3.** Vertical land motion at GNSS stations within the study area taken from Schumacher et al. (2018). Stations depicted are those within 150 km of the coastline to better represent vertical land motion relevant to the RSL sites shown in Fig. 1. Locations of the ten tide gauge stations considered in Section 3.2.2 are indicated by black squares.

outer shell such that it acts as an elastic plate on GIA timescales. Multiple possible values for lithosphere thickness (LT) were considered: 46, 71, 96 and 120 km. The model upper mantle extends from the base of the lithosphere to a depth of 671 km with uniform viscosity, and the model lower mantle extends from 671 km depth to the Core-Mantle boundary at 2885 km depth. The viscosity in the upper and lower mantle regions is assumed uniform with the following range of values considered: upper mantle viscosity (UMV) (0.05, 0.08, 0.1, 0.2, 0.3, 0.5, 0.8, 1.0, 2.0, 3.0, 5.0)  $\times 10^{21}$  Pa and, lower mantle viscosity (LMV) (1, 2, 3, 5, 10, 20, 30, 50, 70, 90)  $\times 10^{21}$  Pa. The elastic and density structure of the Earth model are parameterised with greater depth resolution (ranging from 1 km in the lithosphere to 30 km at the base of the lower mantle) with values taken from seismic constraints (Dziewonski and Anderson, 1981).

A primary input to the GIA model is a reconstruction of global ice thickness evolution during the Late Quaternary. In total, seven ice loading histories were used in this study: ICE-6G.C (Peltier et al., 2015; hereafter referred to as ICE-6G), the global model developed by colleagues at the Australian National University (referred to as the ANU ice model; Lambeck et al., 2014 and references therein), and five models that are the same as ICE-6G but include a different Eurasian ice sheet (EIS) component (Tarasov, 2013). These different EIS models include reconstructions of the Fennoscandian, Barents-Kara, and British-Irish ice sheets. These models with different EIS components were included to quantify the sensitivity of our results to variations in this component of

the global ice model, which is the most proximal to our study region. The mean and standard deviation of these different EIS models are illustrated in Fig. S2. We also show in Fig. S3, the barystatic sea level (i.e., the component associated with meltwater input to the ocean basins; Gregory et al., 2019)) for the two global ice models (ANU and ICE-6G) and ICE-6G with one of the EIS models. There are significant differences in barystatic sea level between the two global models. The EIS had largely deglaciated by the early Holocene, which is reflected in the very similar barystatic curves for ICE-6G compared to ICE-6G with a different EIS component.

We computed RSL changes using a code that solves the generalized sea-level equation (Farrell and Clark, 1976; Mitrovica and Milne, 2003), using the algorithm described in Kendall et al. (2005) but updated to incorporate the effects of GIA-induced changes to the Earth's rotation (Milne and Mitrovica, 1998; Mitrovica et al., 2005).

In total, approximately 3080 model runs were performed to sample the set of ice and Earth parameters defined above.

#### 2.4. Estimating model parameters and uncertainty

The quality of the data-model fit for each of the 3080 parameter sets considered was determined by calculating a misfit value. The optimal model parameter set, within the chosen parameter ranges, is that which results in the minimum data-model misfit. In the case of SLIPs, the misfit was computed by first determining the closest point on the model curve in height and time, and then calculating:

$$\delta_{SLIP} = \sqrt{\frac{\sum_{n=1}^N \left( (\Delta_{RSL,n})^2 / \sigma_{RSL,n}^2 + (\Delta_{t,n})^2 / \sigma_{t,n}^2 \right)}{N}}, \quad (\text{Eqn. 1})$$

where  $\Delta_{RSL,n}$  is the difference between observed and modelled RSL for the  $n^{\text{th}}$  observation, while  $\Delta_{t,n}$  is the equivalent for age, and  $\sigma_{RSL,n}$  and  $\sigma_{t,n}$  are the  $1-\sigma$  observational uncertainty for the RSL and age of each data point. N is the total number of observational data for a given subregion. A simplified version of Eqn. (1), in which time differences were not considered, was used for the case of limiting RSL data (notation as for Equation (1)):

$$\delta_{Lim} = \sqrt{\frac{\sum_{n=1}^N \left( (\Delta_{RSL,n})^2 / \sigma_{RSL,n}^2 \right)}{N}}. \quad (\text{Eqn. 2})$$

In this case, no penalty is incurred if the model value is on the “correct” side of a given limiting point (i.e., above a ML point or below a TL point) within the range of temporal uncertainty (further details are provided in Parang et al., 2024). Since limiting data are one-sided RSL constraints, when the misfit for an entire set of earth parameters is calculated, the contribution from limiting data is weighted by 0.5 to account for the poorer constraint provided by these data:

$$\delta_{Total} = \delta_{SLIP} + 0.5\delta_{Lim}. \quad (\text{Eqn. 3})$$

The misfit for GNSS-determined VLM rates was calculated using an equation that is equivalent to Eqn. (2) but where with the ‘ $\Delta$ ’ represents the difference between the observed and modelled VLM rate, and  $\sigma$  the uncertainty in the VLM observations.

Following Briggs and Tarasov (2013), the RSL and age uncertainties were scaled such that data points with a relatively low density in time and/or space would have a greater weight in the misfit calculation. Specifically, to account for variations in spatial density, we applied

$$\sigma_{RSL,n} = \sqrt{\frac{N_{site}}{N_{total}}} \sigma_{RSL,n}^{\text{orig}}, \quad (\text{Eq. 4})$$

where  $N_{site}$  and  $N_{total}$  are, respectively, the number of data points at a given site and in the entire dataset, and  $\sigma_{RSL,n}^{\text{orig}}$  is the unscaled (original) uncertainty in RSL of the  $n^{\text{th}}$  data point. To account for variations in

temporal density, we applied

$$\sigma_{t,n} = \sqrt{\frac{N_{bin}}{N_{total}}} \sigma_{t,n}^{orig}, \quad (\text{Eq. 5})$$

Where  $N_{bin}$  is the number of data in one of four time bins considered (0–3, 3–6, 6–9, 9+ ka) across all sites and  $\sigma_{t,n}^{orig}$  is the unscaled (original) uncertainty in age of the nth data point. While it is important to include this weighting procedure, we can report that it did not have a significant impact on our results.

Model uncertainty is estimated using the Bayesian approach described in Love et al. (2016; their Section 2.3.2). Since a number of the requirements for accurate application of this approach are not met (Love et al., 2016), it provides only an estimate of the model uncertainty. For a given data set, the probability of a given model parameter set is given by:

$$P(m|d) \propto P(d|m)P(m), \quad (\text{Eqn. 6})$$

where  $P(m|d)$  is the posterior probability of a specific model parameter vector ( $m$ ) for a given data set ( $d$ ),  $P(d|m)$  is the likelihood function and

$P(m)$  is the prior probability of a given parameter vector. For our application, we assume a uniform prior ( $P(m)$ ) and define our likelihood function as:

$$P(d|m) = e^{-\delta^2}, \quad (\text{Eqn. 7})$$

where  $\delta$  is the data-model misfit value for a specified model parameter set.

The posterior probabilities estimated from Equation (6) are normalized so that they sum to unity over the model ensemble. We adopt a 1- $\sigma$  uncertainty threshold (i.e., 68.27 %) to determine a sub-ensemble of the highest-probability model parameter sets. This sub-ensemble is then used to calculate a 1- $\sigma$  range in model output for a given observable (e.g., RSL at model time steps). Therefore, the calculated model bounds generally reflect output from different model parameter sets within the determined (1- $\sigma$ ) sub-ensemble.

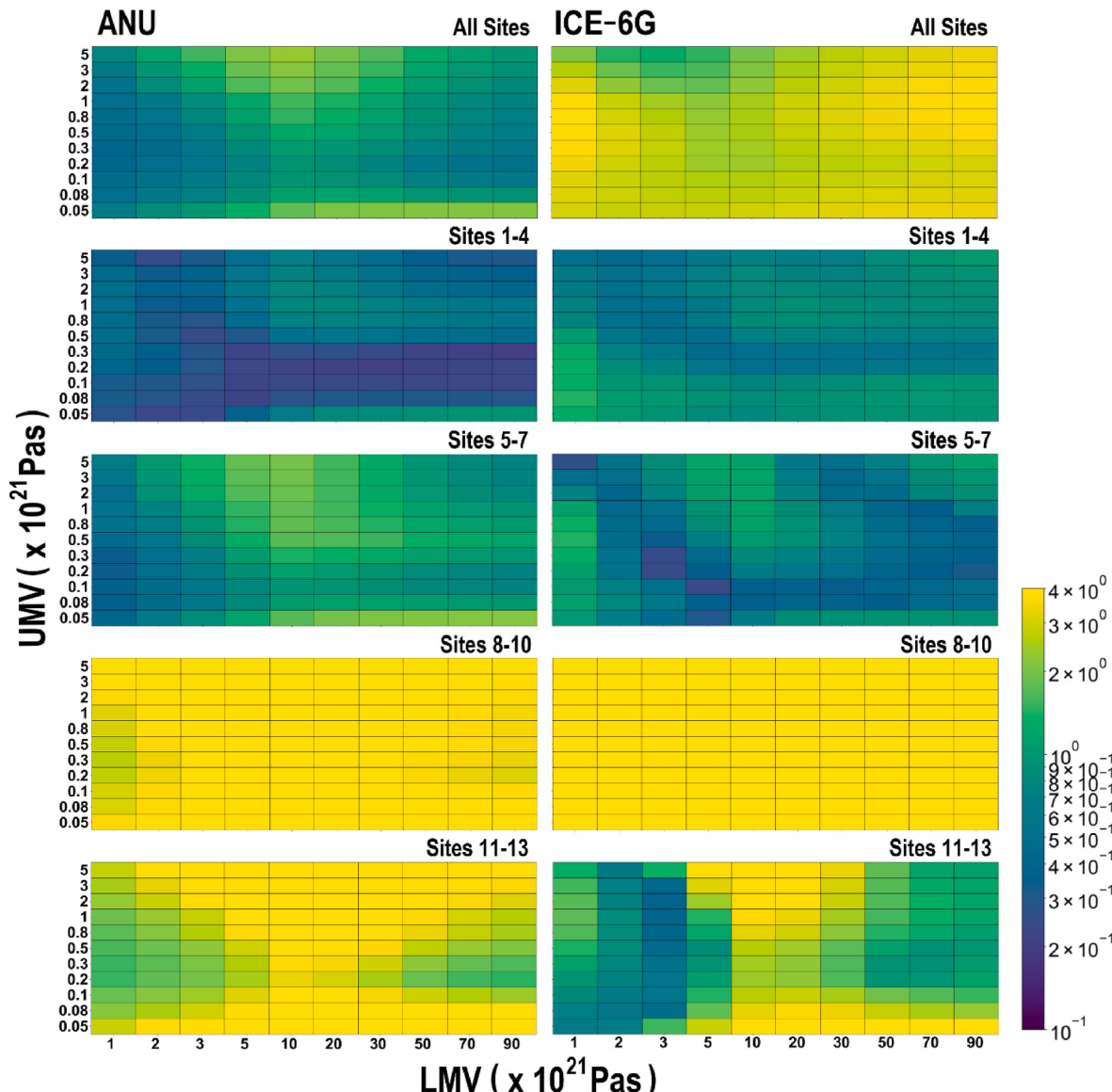


**Fig. 4.** Data model misfit plots for the ANU (left column) and ICE-6G (right column) ice models for the entire data set (top row) and data subsets (as indicated). ANU results are for LT = 71 km; ICE-6G results are for LT = 120 km (respective best fitting values).

### 3. Results and discussion

#### 3.1. Model parameter estimation

**Fig. 4** depicts significant differences in data-model misfit values between global ice history models ANU and ICE-6G. Comparing results for the entirety of the data set (top two frames), the misfit results indicate that the ANU model generally produces better fits compared to ICE-6G for most Earth model parameter sets. Also, the optimal earth model parameter sets are not compatible between the two ice models, with the ICE-6G model producing optimal fits for a region of viscosity space – high values of UMV ( $\sim 3.5 \times 10^{21}$  Pas) and low to average values of LMV ( $\sim 2.5 \times 10^{21}$  Pas) – that produces some of the poorest fits obtained with the ANU model. Model fits for different data sub-regions are also indicated in **Fig. 4**. These show that the quality of fit varies significantly between regions, with misfit values being highest for both models at sites 8–10. They also indicate that the ANU model produces better fits for the sub-regions with sites 1–4 and 8–10, with ICE-6G giving better results for regions with sites 5–7 and 11–13. **Table 1** gives best-fitting sets of Earth parameters and corresponding misfit values for each data set considered in **Fig. 4**. We note that good fits for the ANU model (entire data set) are also produced for Earth models with high LMV values ( $\sim 50.90 \times 10^{21}$  Pas) which is consistent with the findings based on a global analysis of RSL observations (Lambeck et al., 2014).

**Fig. S3** shows misfit values for the ice history model EIS-75954 as compared to the ICE-6G model and shows that changes to the EIS component of the model make relatively minor changes in data-model misfit (similar results were found using the other five EIS models considered (Section 2.3)). This reflects the fact that changes to the thickness distribution of the EIS component of the ice model (**Fig. S2**) have a minor impact on the modelled RSL curves over the study region – with differences of a few decimeters or less during the Holocene (for the same earth model parameters). Thus, the differences apparent in **Fig. 4** are dominated by differences in the barystatic component of the two global ice models. These differences (**Fig. S4**) are significant, varying between  $\sim 3$  m in the mid-Holocene to well over 10 m in the early Holocene. The improved fits for the ANU ice model for the majority of considered earth viscosity models indicates that the Holocene barystatic function in the ANU model is more accurate compared to that for ICE-6G. We further test this conclusion below by considering a subset of the RSL data and GNSS determinations of VLM.

The misfit results (**Fig. 4**) are reflected in **Fig. 5** which shows data-model comparisons using optimal Earth model parameters at each site. Given that the EIS models give results that are very similar to ICE-6G, we consider only one of these five models (75954) for the remainder of this analysis. All ice models fit the SLIP data well at most sites. However, as apparent in **Fig. 4**, the largest data-model misfits occur for sites 8–10 & 11–13. The optimal model curves based on the ICE-6G model (including EIS75954) sit below those for the ANU model during most of the Holocene. This is counter intuitive given the differences between the barystatic component of these two global ice models (**Fig. S4**). It is also in conflict with other studies that have used these models to simulate RSL in intermediate to far-field regions (e.g., Vacchi

et al., 2020), in which the relative height of these model curves better reflect their associated barystatic curves. This difference is primarily a result of our optimal UMV for the ICE-6G model being an order of magnitude larger than the value in the earth model usually partnered with ICE-6G (VM5a; Peltier et al., 2015).

**Figs. S5–S7** explore the data-model misfit for the three data-model subsets (TL, ML, and SLIPs, respectively). These figures show that the ANU model performs well when considering the TL data (**Fig. S5**) but the ICE-6G model produces better results for the ML data at most locations (**Fig. S6**). For the SLIPs, the misfit results are broadly similar between the two models. These three figures show that, although the ANU model best fits the entire dataset, the ICE-6G model can fit the data better for specific data types and sites. For instance, the ANU model often exhibits greater misfits for regions 8–10 and 11–13 for ML (**Fig. S6**) and SLIP (**Fig. S7**) data. While best-fitting earth parameter sets based on ICE-6G may have lower misfits for specific data types at specific sites, when compared to those for the ANU model, the parameter sets that result in optimal fits are quite different for different data types, leading to a total misfit that is generally larger compared to that for the ANU model (**Fig. 4**, top frames).

Since the model sub-ensemble used to define model uncertainty is based on the misfit values (Section 2.4, Eqn. (7)), preference of the RSL data for the ANU model is also evident in this aspect of the analysis. Of the entire ensemble based on three ice models (ANU, ICE-6G, EIS75954; 1320 runs in total), the estimated  $1-\sigma$  sub-ensemble contains 203 sets of model output of which 201 were generated with the ANU model and 2 with the EIS75954 model. This sub-ensemble was used to define the model uncertainty range (dashed lines in **Fig. 5**) by picking the maximum and minimum RSL values from the sub-ensemble at each model time step. Most of the data lie within the calculated uncertainty bounds, although there are some exceptions. For instance, site 6 includes two or three SLIPs that sit above the estimated upper bound around 8–9 ka, and site 10 includes one SLIP at  $\sim 10$  ka that also sits at or above the upper bound. Model uncertainty bounds at site 12 miss three SLIPs, around 2, 8 and 12 ka. These relatively poor results for site 12 are reflected in the (high) misfit results for this site.

**Fig. 6** shows the same results as **Fig. 4** but for the late Holocene (4 ka to present) RSL data subset. This subset was chosen to reduce the influence of differences between ice model barystatic signals (**Fig. S4**) in our estimates of earth viscosity structure. Comparison of **Figs. 4** and **6** shows that the ANU-based misfit results change significantly less than those for the ICE-6G-based results. As expected, the misfit results for this data subset are similar for each ice model, confirming the large impact of the barystatic signal when considering the complete data set. This result also supports our earlier conclusion that the Holocene barystatic component of the ANU model is the more accurate of the two global models considered. One striking feature of the misfit results is the sharp increase for sites 11–13 (lower frames) as LMV increases beyond  $3.5 \times 10^{21}$  Pas for most UMV values. Misfit and RSL curve analysis for sites within this region show site 13 is the primary source of this issue, with RSL curves either intersecting or missing a significant cluster of overlapping SLIPs as LMV values are varied.

A data-model misfit analysis of VLM rates using the data set described in Section 2.2 yields the results in **Fig. 7**. As for the misfit results using late Holocene RSL data (**Fig. 6**), the differences between misfit patterns for all considered ice histories (only those for ANU and ICE-6G shown) are small, indicating that the modelled present-day VLM signal is similar across all three ice models (for each set of Earth model parameters). When comparing the VLM data misfits and those for late Holocene RSL data set (**Fig. 6**, top frames), the similarities are striking in terms of overall pattern and distribution of high and low misfit values, with the one exception being the cluster of higher misfits around UMV  $0.8 \times 10^{21}$  Pas and LMV  $1 \times 10^{21}$  Pas appearing in the GNSS results about equally as strongly as the other two clusters of high misfit values that are apparent for both data sets.

The quality of model fits to the VLM data set is apparent in **Fig. 8**. The

**Table 1**

Summary of lowest misfits across ice models and data sets. Optimum Earth model parameters are given as a triplet: LT – UMV ( $\times 10^{21}$  Pas) – LMV ( $\times 10^{21}$  Pas).

Dataset	Best-Fitting ANU Ice Model & Earth Parameters	Misfit	Best-Fitting ICE-6G Ice Model & Earth Parameters	Misfit
All	ANU 71-0.2-1	0.41	ICE-6G 120-5-3	1.28
1–4	ANU 120-0.2-50	0.18	ICE-6G 46-5-2	0.43
5–7	ANU 46-0.08-1	0.27	ICE-6G 96-0.1-5	0.24
8–10	ANU 46-0.1-1	2.14	ICE-6G 120-5-5	7.45
11–13	ANU 46-0.2-1	1.33	ICE-6G 46-3-3	0.38

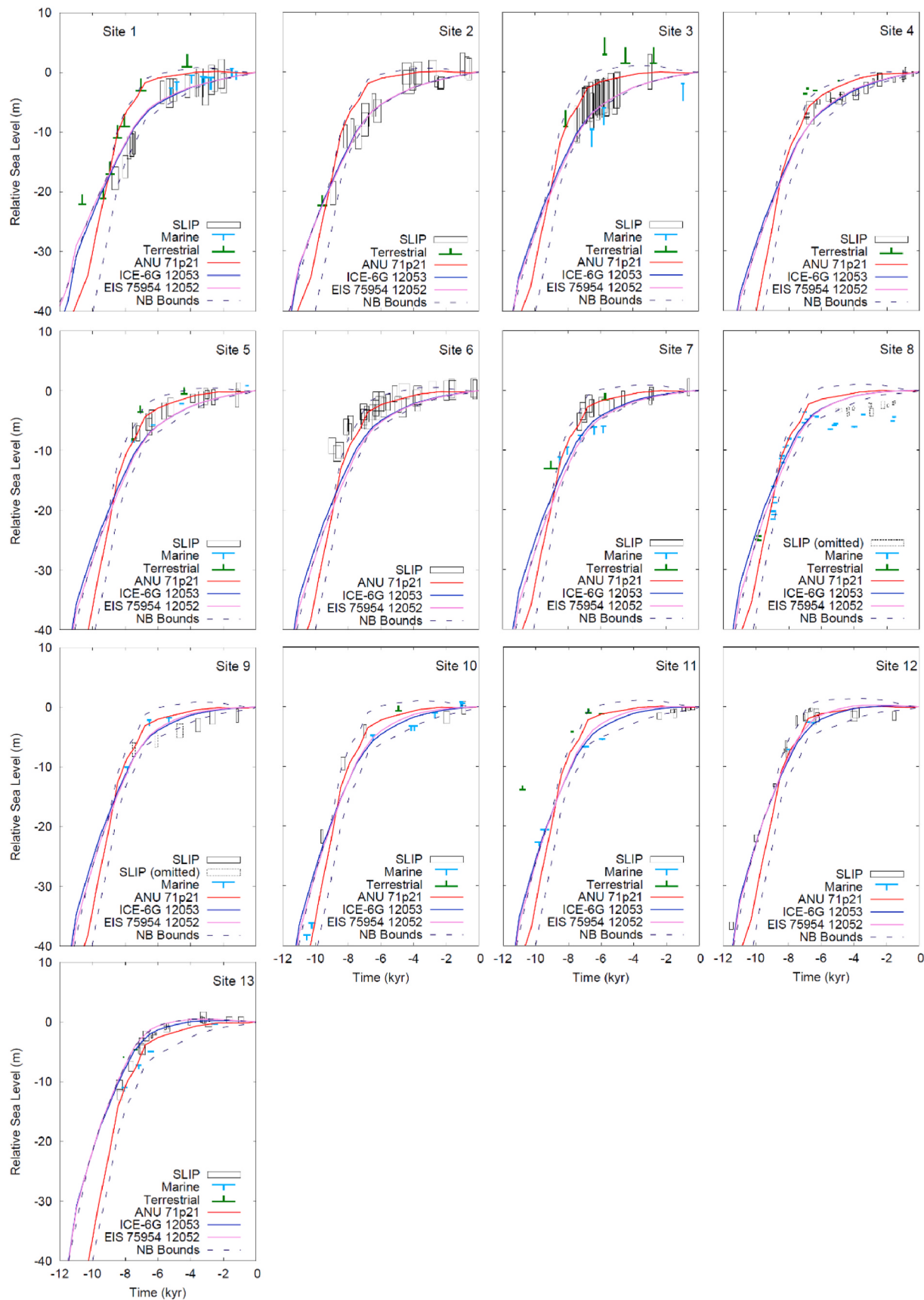


**Fig. 5.** Data-model comparison by site for entire RSL dataset and optimal Earth model parameters for entire data set for three ice models (ANU, ICE-6G, and EIS75954) and estimated 1- $\sigma$  uncertainty bounds (see key for details).

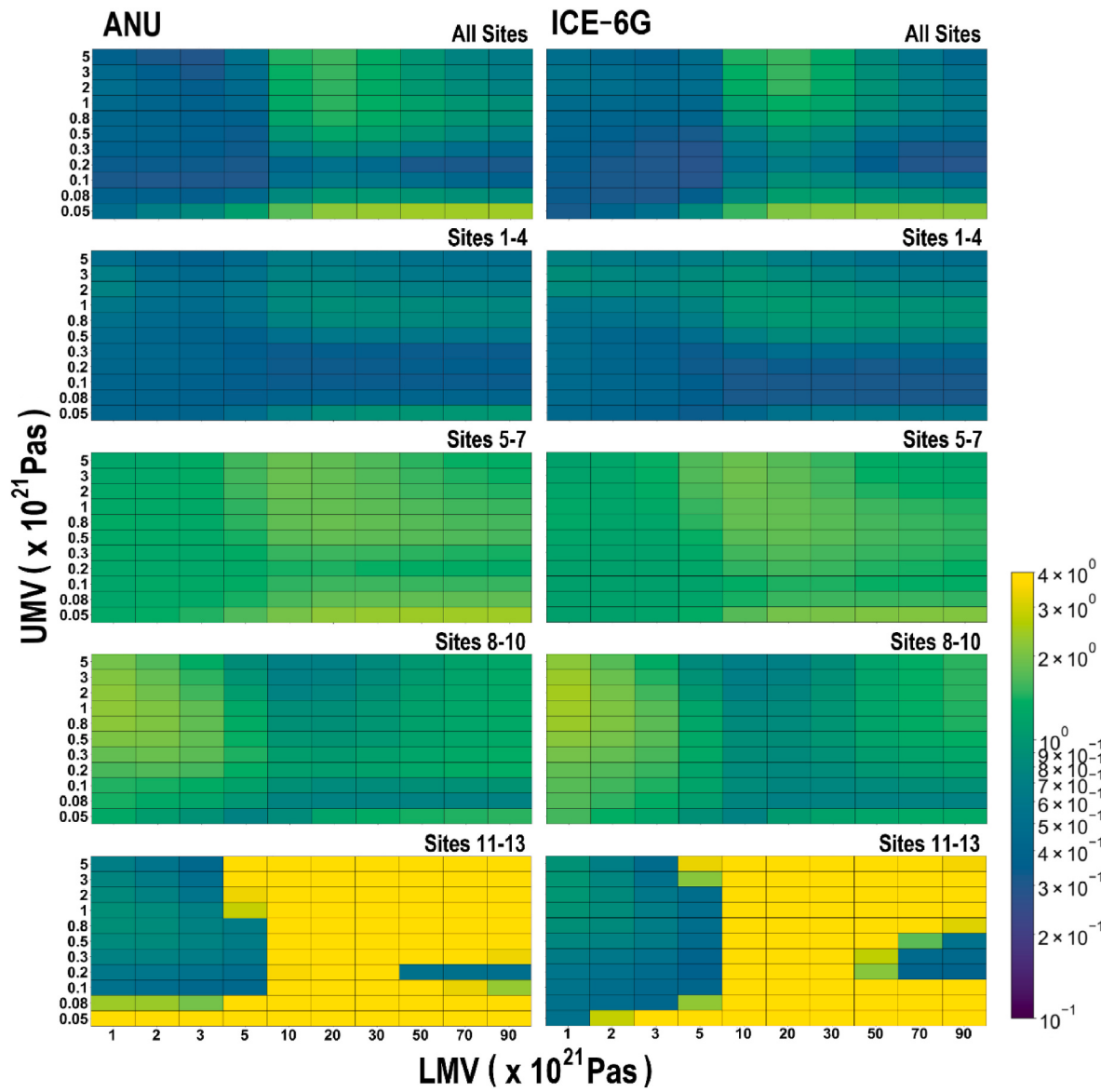


**Fig. 6.** Data-model misfit plots calculated using only RSL data spanning the past 4 ka. ANU results are for LT = 71 km, ICE-6G are for LT = 120 km (respective best fitting LT values).

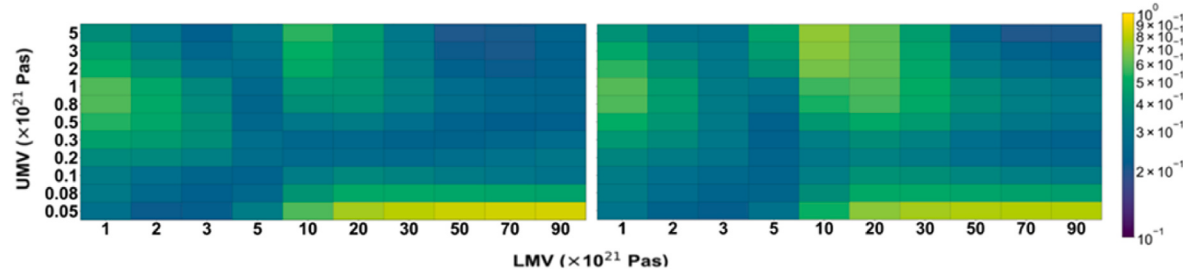


**Fig. 7.** Data-model misfit plots for GNSS data from stations within 150 km of coast (Fig. 3). Results shown for ANU (left) and ICE-6G (right) ice models. These results are based on  $1\sigma$  data uncertainties to be compatible with the RSL analysis.

data-model residuals (observed rate minus model rate) indicate that there is no apparent long-wavelength spatial gradient to within data precision, indicating no strong evidence for lateral variations in Earth viscosity structure. Over 90 % of the optimal model results are within the observed  $2\sigma$  VLM range. The residuals indicate substantial scatter at short spatial scales which most likely reflects data uncertainty as well as

signals associated with local processes (e.g., sediment compaction) and/or site effects (e.g., GNSS antenna monumentation). The most spatially coherent residual is a cluster of negative ( $1-3\sigma$ ) values in the northeastern-most quadrant of the study area (the French coastline along the English Channel), and what may be interpreted as an area of positive residuals in northwestern Spain. An alternative illustration of

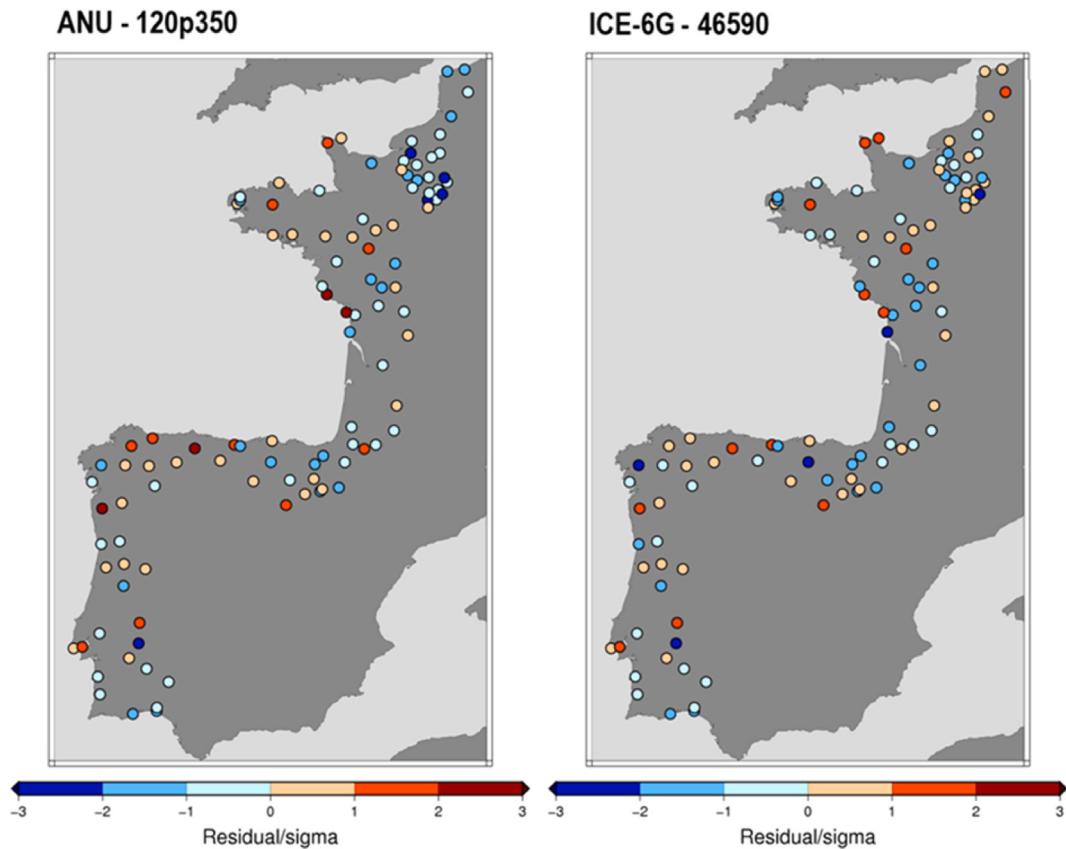


**Fig. 8.** Residual plots for best fitting Earth model parameters for GNSS sites within 150 km of coastline. Earth model parameters are those that best fit the combined GNSS and 4ka RSL datasets (ANU: 120-0.3-50, ICE-6G: 46-5-90).

the data-model fits is provided in Fig. S8, which includes both data and model uncertainty. Overall, the model is compatible with the observations to within data and model uncertainty at long wavelengths but there are some significant residuals in localised areas that warrant further investigation. We provide model output of VLM as supplementary data (see Appendix) for all GNSS stations shown in Figs. 8 & S8. <http://geodesy.unr.edu/NGLStationPages/gpsnetmap/GPSNetMap.html>

Since the misfit results for the late Holocene RSL and GNSS data sets are broadly consistent, we generated results for these data sets combined (Fig. S9) to determine a more robust estimate of optimal Earth model parameters and uncertainty bounds. These results indicate that good fits can be obtained with a single set of Earth model parameters regardless of the chosen ice model. However, there is clearly a considerable degree of non-uniqueness in defining an optimal model parameter set, as is often the case in GIA inversion problems. For example, the minimum misfit for the ANU model (1.6) was achieved with 120-0.3-50, compared to a value of 1.48 with 46-5-70 for the EIS75954 ice model. Compared to the results that considered only the complete set of RSL observations, in which the sub-ensemble of best-fitting models (203 out of 1320 parameter sets) was dominated by the ANU ice model, the uncertainty results based on the combined late Holocene RSL data (4-0 ka) and VLM rates comprise a sub-ensemble of 108 parameter sets in which the three different ice models (ANU, ICE-6G, ICE-6G + EIS75954) appear a similar number of times, indicating no significant bias related to the barystatic signal. The model uncertainty bounds for RSL during the late Holocene are shown with the optimal model curves and the RSL observations in Fig. S10. Generally, the model curves capture the data to within the estimated uncertainty ranges. However, there are a few exceptions, such as some low-lying SLIPs at sites 9, 11 and 12, and some anomalously high ML data points at sites 5 and 10. These data lying beyond model uncertainty bounds suggest that, for the case of SLIPs, sediment

compaction might be a greater issue than identified in previous studies (e.g., García-Artola et al., 2018).

### 3.2. General discussion and model applications

#### 3.2.1. Comparison to previous work

The results of Leorri et al. (2012) and García-Artola et al. (2018) share similarities and differences to the work presented here. The focus of these studies was more on the RSL reconstructions with comparison to GIA model output being of secondary importance. For this reason, a much smaller number of model parameter sets were considered in these studies (7 in Leorri et al. (2012) and 1 in García-Artola et al. (2018)). Also, the RSL data set considered here (and in García-Artola et al., 2018), is considerably more extensive than that considered in Leorri et al. (2012). Our more in-depth modelling analysis supports these previous studies in that the reconstructed RSL changes in this region are largely governed by peripheral bulge subsidence (glacio-isostasy) and continental levering (hydro-isostasy). The contributions of these GIA processes are plotted in Fig. 9 for a model parameter set that fit well the (total) RSL data set and the combined late Holocene RSL and VLM data set (specifically: ANU ice model with LT = 120 km, UMV =  $3 \times 10^{20}$  Pas, LMV =  $5 \times 10^{22}$  Pas (i.e., 120-0.3-50)). These model results indicate that RSL was lower in all parts of the study region at the model time step shown (6.8 ka), with a spatial variation of ~3.5 m along the coastal areas spanned by the RSL reconstructions considered here. The rise in RSL since 6.8 ka was primarily driven by peripheral bulge subsidence in most areas, although continental levering was considerable in some regions, such as northwestern France and Spain, and southern Portugal.

The results in Fig. 9 vary as a function of model parameters but the general pattern and conclusions remain the same. This is evident when comparing our Fig. 9 to Leorri et al. (2012) (their Fig. 4). The primary

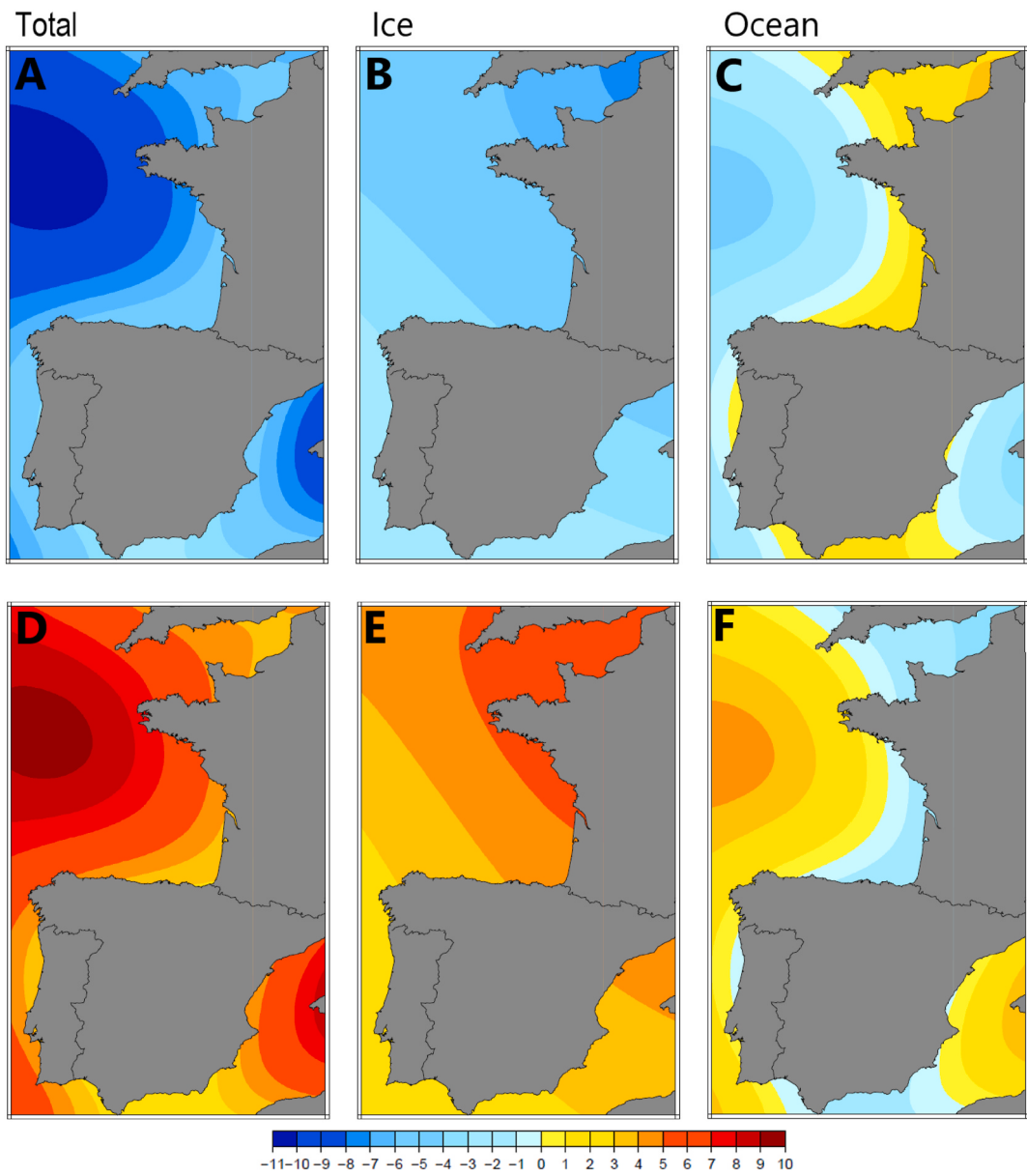


**Fig. 9.** Model output of RSL (top row; A-C) and relative land height (bottom row; D-F) at 6.8 ka for the ANU ice model and earth model parameter set 120-0.3-50. Results are provided for the total signal (A, D) as well as that associated with only ice (B, E) or ocean (C, F) loading. Units are in meters.

differences are a larger continental levering signal due to the lower LT (71 km) used in generating Fig. 4 of [Leorri et al. \(2012\)](#) and the orientation of the RSL gradient associated with glacio-isostasy, reflecting the different ice models being used in each case. As a third point of comparison, we include model output of these component signals for a parameter set that is favoured by the combined late Holocene and GNSS VLM data set ([Fig. S11](#); LT = 71 km, UMV =  $5 \times 10^{21}$  Pas, LMV =  $7 \times 10^{22}$  Pas (i.e., 71-5-70)). In this case, the significantly greater UMV (compared to results in [Fig. 9](#)) leads to much lower rates of deformation and therefore RSL changes that are approximately 50 % of those shown in [Fig. 9](#). These results demonstrate that variations in earth model parameters to within the estimated parametric uncertainty can have a significant impact on the modelled RSL changes.

A key contribution of this work is the determination of model uncertainty. While it can be useful to define an ‘optimal’ parameter set for a given data set, it is more important to define model bounds or uncertainty ranges to better illustrate the primary data-model misfits and highlight model shortcomings for future development and improvement. Furthermore, providing a range of model output that spans model

uncertainty is more useful for end users seeking to include or remove the GIA signal as part of a different analysis (i.e., include it as part of a sea-level budget analysis (Section 3.2.2, below), or remove it to consider signals from other processes). In terms of fitting the RSL data, the primary challenge is to fit SLIPs that sit relatively high in the early Holocene while also fitting SLIPs that sit relatively low in the mid-to-late Holocene ([Goslin et al., 2015](#); [García-Artola et al., 2018](#)). Consideration of model uncertainty can address many of the data-model misfits noted previously – specifically, high early Holocene RSL at sites 4, 10, 12 & 13 and low late Holocene RSL at sites 8, 9, & 11. We reiterate that at least some of these late Holocene data-model discrepancies are likely associated with processes that operate on shorter spatial scales than GIA, such as sediment compaction (e.g., [García-Artola et al., 2018](#); [Li et al., 2024](#)). Even when considering model uncertainty (dashed lines in [Fig. 5](#)), there remain some misfits as noted in Section 3.1, but they are relatively minor.

In terms of reducing model uncertainty, our results suggest that improving constraints on the barystatic signal (as defined by the global ice history model) would be a logical first target as this would lead to

improved constraints on earth model parameters. This aspect of the model is a primary contributor to the spread in the model uncertainty ranges. As noted above, our results indicate that the barystatic component of the ANU ice model is more accurate than that for ICE-6G. This is supported by two results from our analysis: (i) the ANU model is in the majority of accepted parameter sets when considering the complete RSL data set, and (ii) misfit results for the ANU model when late Holocene RSL and/or GNSS VLM data sets are considered do not vary significantly compared to those for the full RSL data set. This conclusion aligns well with that of Goslin et al. (2015) who identified error in the barystatic signal as being a possible explanation for data-model misfits in north-western France. They also suggested that uncertainty in the EIS could be a primary source of misfit. Our results based on the 5 different regional EIS models embedded in the global ICE-6G model indicate that uncertainty in this aspect of the model plays a relatively minor role when considering Holocene RSL in the study region.

### 3.2.2. Sea-level budget analysis

In this sub-section, we apply our new GIA model constraints in a sea-level budget analysis focusing on the latter half of the 20th century, specifically, the 40-yr period 1957 to 1997. This period was chosen as it pre-dates most of the satellite era and there are published constraints on the non-GIA signals that contribute to the observed sea-level response. Specifically, we adopt signals associated with changes in land ice (Greenland ice sheet (GIS), Antarctic ice sheet (AIS), glaciers), and changes in terrestrial water storage (TWS) from Frederikse et al. (2020). For the sterodynamic (sdyn) signal, we adopt the results from Dangendorf et al. (2024). Only 10 tide gauge stations from our study region (Fig. 3) spanned the chosen time interval with relatively continuous data coverage. For these stations, we isolated the time series for each of the component signals and performed the best linear unbiased estimation (Johnson and Wichern, 2007) to determine the rate and its uncertainty.

Our sea-level budget analysis is based on the following definition of the modelled rate of RSL (RRSL):

$$\begin{aligned} RRSL_{\text{mod}} = & RRSL_{\text{sdyn}} + RRSL_{\text{AIS}} + RRSL_{\text{GIS}} + RRSL_{\text{glaciers}} + RRSL_{\text{TWS}} \\ & + RRSL_{\text{GIA}} \end{aligned} \quad (\text{Eqn. 8})$$

where each term represents the different component signals noted above. The difference between  $RRSL_{\text{mod}}$  and the observed rate will

reflect a bias in one or more of the component estimates or an unmodelled process.

The measured and modelled rates are depicted in Fig. 10 and provided in Table S1. The sterodynamic component is largest at all sites. The uncertainty for this component is also larger than that for all other component signals except for GIA. Glacier melting and GIA are the next two most important signals, with comparable amplitudes at most sites (although the GIA signal is more spatially variable, ranging from 0.3 to 0.7 mm/yr). Therefore, GIA is clearly an important contributor to 20th century RSL rise in this region and so should be included in estimates of past and future RSL change (Leorri et al., 2012; Simon et al., 2021; Hammond et al., 2021). Our estimates of the GIA uncertainty are of similar amplitude to the total signal. This result reflects the precision of the data sets considered and the ability of our model to capture the observed signals (quantified by the misfit values). We note that our estimates of the GIA model uncertainty are considerably larger than those determined in a recent analysis for the Mediterranean region (Spada and Melini, 2022).

The results in Fig. 10 indicate that the sea-level budget is not closed at 7 of the 10 stations considered. Even if a more conservative  $2\sigma$  uncertainty is adopted, the residual signal is non-zero at stations Dieppe, La Coruna I, Leixoes, and Cascais. Dieppe shows the largest residual, with an amplitude of almost 4 mm/yr. Such a large amplitude suggests the contribution from an unmodelled VLM signal. However, there are several GNSS stations in close proximity to this tide gauge station and taking a weighted average of these gives a VLM rate of  $-1.037 \pm 0.251$  (Hammond et al., 2021; see also <https://geodesy.unr.edu/vlm.php>). Therefore, this anomalous signal appears to be linked to highly localized subsidence at the site of the tide gauge (as supported by information provided by the Permanent Service for Mean Sea Level; see <https://psmsl.org/data/obtaining/stations/474.php#docu>).

GIA model output of RSL rates at all tide gauge sites in our study region is provided as supplementary data (see Appendix).

## 4. Conclusions

Our results extend past work that considered RSL observations and the GIA contribution to the observed changes along the Atlantic coast of Europe (Leorri et al., 2012; Goslin et al., 2015; García-Artola et al., 2018). We present model results generated using seven ice history models and 440 Earth models (3080 GIA model parameter sets in total).

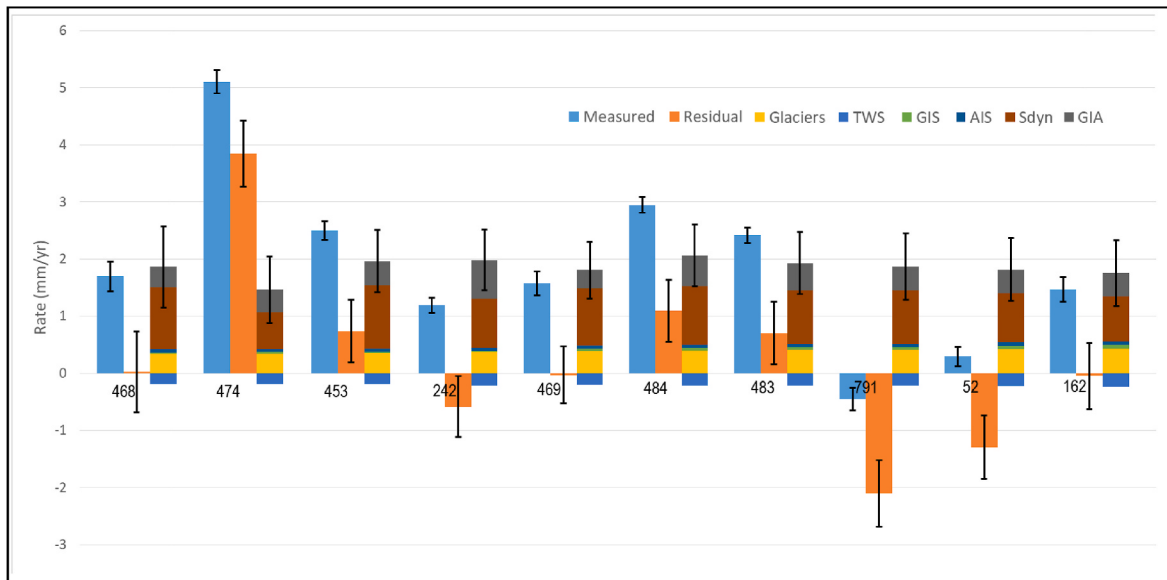


**Fig. 10.** Estimated component RSL signals (right column at each site), the linear trend determined from annual tide gauge data (left column), and the difference between these (measured minus sum of component signals; middle column). Indicated uncertainties are  $1\sigma$ .

With this broad range of parameter values, good quality model fits to the Holocene RSL data were obtained. The best-fitting Earth model parameter sets varied considerably when two different global ice history models (ICE-6G and ANU) were applied, indicating the sensitivity of the Earth model parameter inferences to the barystatic component of the ice model. In contrast, our results show that predictions of Holocene RSL in this region are relatively insensitive to variations in the thickness distribution of the EIS. Plausible variations in this component of the ice model generally resulted in small (few decimeters) changes in RSL and thus made little impact on earth model parameter estimation.

To reduce the dependency of our earth model parameter estimation on the barystatic component of the adopted ice model, a temporal subset of the RSL data was considered (past 4 ka) as well as observations of VLM with non-GIA signals removed. Using these data sets, a more robust inference of Earth model parameters was obtained. The results for these two data sets also indicate that the barystatic component of the ANU model is more accurate than that of the ICE-6G model during the Holocene.

Model uncertainty was determined using data-model misfit values and a Bayesian approach to define a subset of parameter sets at the  $1\sigma$  confidence level. When considering the model uncertainty, 95 % of the Holocene RSL observations can be explained. There remain a small number of exceptions, particularly during the late Holocene in northern Spain, where a number of SLIPs fall below the model uncertainty range. These residuals are most likely due to localised processes unrelated to GIA (Leorri et al., 2012; García-Artola et al., 2018; Li et al., 2024). The majority (93 %) of the VLM data set (Schumacher et al., 2018) can also be explained when considering model uncertainty, with 8 sites out of 107 lying outside the GIA model uncertainty range. However, there are some areas, notably northern France and Spain, where there are spatially coherent residuals, suggesting the importance of contemporary signals.

Our results support previous work in showing that GIA-related subsidence along the Atlantic coast of Europe is dominated by ice-(un)loading (peripheral bulge) effects and that ocean loading is also important in some areas, such as northwestern France. The amplitude of these effects is strongly dependent on the chosen Earth model parameters. Using our subset of best-fitting parameter sets, we performed a sea-level budget analysis for the period 1957 to 1997 using data from 10 tide gauges in our study region. Using estimates of non-GIA signals, we find that the stereodynamic signal is the largest contributor at most of the considered tide gauge sites, with signals due to GIA and glaciers the next largest. The GIA signal dominates the uncertainty in modelled sea level rise at all sites. Of the 10 tide gauge stations considered, the budget is closed at six (to within  $2\sigma$  uncertainty). The largest residual was found for the station Dieppe in northern France, with an unexplained signal of  $3.8 \pm 0.6$  mm/yr, suggesting a large unmodelled signal at this location (most likely related to localized subsidence at the tide gauge site). We provide GIA model output (including uncertainty) for rates of VLM and RSL at, respectively, GNSS and tide gauge stations in our study region (see Appendix).

## Author contributions

GC led the research and writing of the manuscript. GAM designed the study, supervised GC in performing the research and in writing the manuscript. SP, PA, RL and AG contributed to certain aspects of the analysis and interpretation of results and contributed to writing the manuscript. LT provided ice history models of the Eurasian ice sheet and contributed to writing the manuscript.

## Declaration of competing interest

The authors declare that they have no known competing financial interests or personal relationships that could have appeared to influence the work reported in this paper.

## Acknowledgements

GC acknowledges financial support from the University of Ottawa. GAM acknowledges funding support from the Natural Sciences and Engineering Research Council (NSERC) of Canada (Discovery Grant RGPIN-2024-06439). We thank Ane Garcia-Artola for guidance in recalibrating some of the ages in the sea-level dataset. We thank Matteo Vacchi and two anonymous reviewers for providing constructive feedback that improved the quality of this paper.

## Appendix A. Supplementary data

Supplementary data to this article can be found online at <https://doi.org/10.1016/j.quascirev.2025.109577>.

## Data availability

A link to the data and/or code is provided as part of this submission.

## References

- Bradley, S.L., Ely, J.C., Clark, C.D., Edwards, R.J., Shennan, I., 2023. Reconstruction of the palaeo-sea level of Britain and Ireland arising from empirical constraints of ice extent: implications for regional sea level forecasts and North American ice sheet volume. *J. Quat. Sci.* 38, 791–805. <https://doi.org/10.1002/jqs.3523>.
- Briggs, R.D., Tarasov, L., 2013. How to evaluate model-derived deglaciation chronologies: a case study using Antarctica. *Quat. Sci. Rev.* 63, 109–127. <https://doi.org/10.1016/j.quascirev.2012.11.021>.
- Clark, J.A., Farrell, W.E., Peltier, W., 1978. Global changes in postglacial sea level: a numerical calculation. *Quat. Res. (Tokyo)* 9 (3), 265–287. [https://doi.org/10.1016/0033-5894\(78\)90033-9](https://doi.org/10.1016/0033-5894(78)90033-9).
- Clark, P.U., Dyke, A.S., Shakun, J.D., Carlson, A.E., Clark, J., Wohlfarth, B., Mitrovica, J.X., Hostetler, S.W., McCabe, A.M., 2009. The last glacial maximum. *Science* 325, 710–714. <https://doi.org/10.1126/science.117287>.
- Dangendorf, S., Sun, Q., Wahl, T., Thompson, P., Mitrovica, J.X., Hamlington, B., 2024. Probabilistic reconstruction of sea-level changes and their causes since 1900. *Earth Syst. Sci. Data* 16, 3471–3494. <https://doi.org/10.5194/essd-16-3471-2024>.
- Davis, J.L., Mitrovica, J.X., 1996. Glacial isostatic adjustment and the anomalous tide gauge record of eastern North America. *Nature* 379, 331–333. <https://doi.org/10.1038/379331a0>.
- Dziewonski, A.M., Anderson, D.L., 1981. Preliminary reference Earth model. *Phys. Earth Planet. Inter.* 25 (4), 297–356. [https://doi.org/10.1016/0031-9201\(81\)90046-7](https://doi.org/10.1016/0031-9201(81)90046-7).
- Engelhart, S.E., Horton, B.P., Douglas, B.C., Peltier, W.R., Törnqvist, T.E., 2009. Spatial variability of late Holocene and 20th century sea-level rise along the Atlantic coast of the United States. *Geology* 37 (12), 1115–1118. <https://doi.org/10.1130/G30360A.1>.
- Farrell, W.E., Clark, J.A., 1976. On postglacial sea level. *Geophys. J. Int.* 46 (3), 647–667. <https://doi.org/10.1111/j.1365-246X.1976.tb01252.x>.
- Fox-Kemper, B., Hewitt, H.T., Xiao, C., Aðalgeirsdóttir, G., Drijfhout, S.S., Edwards, T.L., Golledge, N.R., Hemer, M., Kopp, R.E., Krinner, G., Mix, A., Notz, D., Nowicki, S., Nurhati, I.S., Ruiz, L., Sallée, J.-B., Slagter, A.B.A., Yu, Y., 2021. Ocean, cryosphere and sea level change. In: Masson-Delmotte, V., Zhai, P., Pirani, A., Connors, S.L., Péan, C., Berger, S., Caud, N., Chen, Y., Goldfarb, L., Gomis, M.I., Huang, M., Leitzell, K., Lonnoy, E., Matthews, J.B.R., Maycock, T.K., Waterfield, T., Yelekçi, O., Yu, R., Zhou, B. (Eds.), *Climate Change 2021: the Physical Science Basis. Contribution of Working Group I to the Sixth Assessment Report of the Intergovernmental Panel on Climate Change*. Cambridge University Press, Cambridge, United Kingdom and New York, NY, USA, pp. 1211–1362. <https://doi.org/10.1017/9781009157896.011>.
- Frederikse, T., Landerer, F., Caron, L., Adhikari, S., Parkes, D., Humphrey, V.W., Dangendorf, S., Hogarth, P., Zanna, L., Cheng, L., Wu, Y.-H., 2020. The causes of sea-level rise since 1900. *Nature* 584, 393–397. <https://doi.org/10.1038/s41586-020-2591-3>.
- García-Artola, A., Stéphan, P., Cejarreta, A., Kopp, R.E., Khan, N.S., Horton, B.P., 2018. Holocene sea-level database from the Atlantic Coast of Europe. *Quat. Sci. Rev.* 196, 177–192. <https://doi.org/10.1016/j.quascirev.2018.07.031>.
- Gehrels, W.R., Dawson, D.A., Shaw, J., Marshall, W.A., 2011. Using Holocene relative sea-level data to inform future sea-level predictions: an example from southwest England. *Global Planet. Change* 78, 116–126. <https://doi.org/10.1016/j.gloplacha.2011.05.013>.
- Goslin, J., Van Vliet-Lanoë, B., Spada, G., Bradley, S., Tarasov, L., Neill, S., Suárez, S., 2015. A new Holocene relative sea-level curve for Western Brittany (France): insights on isostatic dynamics along the Atlantic coasts of north-western Europe. *Quat. Sci. Rev.* 129, 341–365. <https://doi.org/10.1016/j.quascirev.2012.100851>.
- Gregory, J.M., Griffies, S.M., Hughes, C.W., et al., 2019. Concepts and terminology for sea level: mean, variability and change, both local and global. *Surv. Geophys.* 40, 1251e1289. <https://doi.org/10.1007/s10712-019-09525-z>.
- Hammond, W.C., Blewitt, G., Kreemer, C., Nerem, R.S., 2021. GPS imaging of global vertical land motion for studies of sea level rise. *J. Geophys. Res. Solid Earth* 126, e2021JB022355. <https://doi.org/10.1029/2021JB022355>.

- Heaton, T., Köhler, P., Butzin, M., Bard, E., Reimer, R., Austin, W., Bronk Ramsey, C., Grootes, P., Hughen, K., Kromer, B., Reimer, P., Adkins, J., Burke, A., Cook, M., Olsen, J., Skinner, L., 2020. Marine20 - the marine radiocarbon age calibration curve (0–55,000 cal BP). Radiocarbon 62. <https://doi.org/10.1017/RDC.2020.68>.
- James, T.S., Gowan, E.J., Hutchinson, I., Clague, J.J., Barrie, J.V., Conway, K.W., 2009. Sea-level change and paleogeographic reconstructions for southern Vancouver Island, British Columbia, Canada. Quat. Sci. Rev. 28 (13–14), 1200–1216. <https://doi.org/10.1016/j.quascirev.2008.12.022>.
- Johnson, R.A., Wichern, D.W., 2007. Applied Multivariate Statistical Analysis, sixth ed. Pearson Education Ltd, Upper Saddle River, New Jersey, 07458.
- Karegar, M.A., Dixon, T.H., Engelhart, S.E., 2016. Subsidence along the Atlantic Coast of North America: insights from GPS and late Holocene relative sea level data. Geophysical Research Letters 43, 3126–3133. <https://doi.org/10.1002/2016GL068015>.
- Kendall, R.A., Mitrovica, J.X., Milne, G.A., 2005. On post-glacial sea level – II. Numerical formulation and comparative results on spherically symmetric models. Geophys. J. Int. 161 (3), 679–706.
- Khan, N.S., Ashe, E., Shaw, T.A., Vacchi, M., Walker, J., Peltier, W.R., Kopp, R.E., Horton, B.P., 2015. Holocene relative sea-level changes from Near-, Intermediate-, and far-field locations. Curr. Clim. Change Rep. 1, 247–262. <https://doi.org/10.1007/s40641-015-0029-z>.
- Khan, N.S., Horton, B.P., Engelhart, S., Rovere, A., Vacchi, M., Ashe, E.L., Törnqvist, T.E., Dutton, A., Hijma, M.P., Shennan, I., the HOLSEA working group, 2019. Inception of a global atlas of sea levels since the last glacial maximum. Quat. Sci. Rev. 220, 359–371. <https://doi.org/10.1016/j.quascirev.2019.07.016>.
- Lambeck, K., Rouby, H., Purcell, A., Sun, Y., Cambridge, M., 2014. Sea level and global ice volumes for the last glacial maximum to the Holocene. Earth, Atmospheric, and Planetary Sciences 111 (43), 15296–15303. <https://doi.org/10.1073/pnas.1411762111>.
- Lambeck, K., Bard, E., 2000. Sea-level change along the French Mediterranean coast for the past 30 000 years. Earth Planet Sci. Lett. 175, 203–222. [https://doi.org/10.1016/S0012-821X\(99\)00289-7](https://doi.org/10.1016/S0012-821X(99)00289-7).
- Lambeck, K., Smither, C., Johnston, P., 1998. Sea-level change, glacial rebound and mantle viscosity for northern Europe. Geophys. J. Int. 134, 102–144. <https://doi.org/10.1046/j.1365-246x.1998.00541.x>.
- Leorri, E., Cebrero, A., Milne, G., 2012. Field observations and modelling of Holocene sea-level changes in the southern Bay of Biscay: implications for understanding current rates of relative sea-level change and vertical land motion along the Atlantic coast of SW Europe. Quat. Sci. Rev. 42, 59–73. <https://doi.org/10.1016/j.quascirev.2012.03.014>.
- Li, T., García-Artola, A., Shaw, T.A., et al., 2024. Vertical land motion is underestimated in sea-level projections from the Oka Estuary, northern Spain. Sci. Rep. 14, 31302. <https://doi.org/10.1038/s41598-024-82692-1>.
- Li, T., Wu, P., Wang, H., Steffen, H., Khan, N.S., Engelhart, S.E., Vacchi, M., Shaw, T.A., Peltier, W.R., Horton, B.P., 2020. Uncertainties of glacial isostatic adjustment model predictions in North America associated with 3D structure. Geophys. Res. Lett. 1–10. <https://doi.org/10.1029/2020GL087944>.
- Love, R., Milne, G.A., Tarasov, L., Engelhart, S.E., Hijma, M.P., Latychev, K., Horton, B.P., Törnqvist, T.E., 2016. The contribution of glacial isostatic adjustment to projections of sea-level change along the Atlantic and Gulf coasts of North America. Earths Future 4, 440–464. <https://doi.org/10.1002/2016EF000363>.
- Milne, G.A., Mitrovica, J.X., 1998. Postglacial sea-level change on a rotating Earth. Geophys. J. Int. 133 (1), 1–19.
- Mitrovica, J.X., Milne, G.A., 2003. On post-glacial sea level: I. General theory. Geophys. J. Int. 154, 253–267.
- Mitrovica, J.X., Wahr, J., Matsuyama, I., Paulson, A., 2005. The rotational stability of an ice-age Earth. Geophys. J. Int. 161 (2), 491–506. <https://doi.org/10.1111/j.1365-246X.2005.02609.x>.
- Muhs, D.R., Simmons, K.R., Schumann, R.R., Groves, L.T., Mitrovica, J.X., Laurel, D.A., 2012. Sea-level history during the Last interglacial complex on San Nicolas Island California: implications for glacial isostatic adjustment processes, paleoceanography and tectonics. Quat. Sci. Rev. 31, 1–25. <https://doi.org/10.1016/j.quascirev.2012.01.010>.
- Parang, S., Milne, G.A., Yousefi, M., Tarasov, L., Latychev, K., 2024. Constraining models of glacial isostatic adjustment in eastern North America. Quat. Sci. Rev. 334, 108708. <https://doi.org/10.1016/j.quascirev.2024.108708>.
- Park, K., Nerem, R.S., Davis, J.L., Schenewerk, M.S., Milne, G.A., Mitrovica, J.X., 2002. Investigation of glacial isostatic adjustment in the northeast U.S. using GPS measurements. Geophys. Res. Lett. 29 (11), 1509. <https://doi.org/10.1029/2001GL013782>.
- Peltier, W.R., 1974. The impulse response of a Maxwell Rheology Earth. Rev. Geophys. 12 (4), 649–669. <https://doi.org/10.1029/RG012i004p00649>.
- Peltier, W.R., 1996. Mantle viscosity and ice-age ice sheet topography. Science 273 (5280), 1359–1364. <https://doi.org/10.1126/science.273.5280.1359>.
- Peltier, W.R., 2004. Global glacial isostasy and the surface of the ice-age Earth: the ICE-5G (VM2) model and GRACE. Annu. Rev. Earth Planet Sci. 32, 111–149. <https://doi.org/10.1146/annurev.earth.32.082503.144359>.
- Peltier, W.R., Argus, D.F., Drummond, R., 2015. Space geodesy constrains ice-age terminal deglaciation: the global ICE-6G C(VM5a) model. J. Geophys. Res. Solid Earth 120, 450–487. <https://doi.org/10.1002/2014JB011176>.
- Reimer, P., Austin, W., Bard, E., Bayliss, A., Blackwell, P., Bronk Ramsey, C., Butzin, M., Cheng, H., Edwards, R., Friedrich, M., Grootes, P., Guilderson, T., Hajdas, I., Heaton, T., Hogg, A., Hughen, K., Kromer, B., Manning, S., Muscheler, R., Palmer, J., Pearson, C., van der Plicht, J., Reimer, R., Richards, D., Scott, E., Southon, J., Turney, C., Wacker, L., Adolphi, F., Büntgen, U., Capino, M., Fahrni, S., Fogtmann-Schulz, A., Friedrich, R., Köhler, P., Kudsk, S., Miyake, F., Olsen, J., Reinig, F., Sakamoto, M., Sookdeo, A., Talamo, S., 2020. The IntCal20 Northern Hemisphere radiocarbon age calibration curve (0–55 cal kBP). Radiocarbon 62 (4), 725–757. <https://doi.org/10.1017/RDC.2020.41>.
- Roy, K., Peltier, W.R., 2015. Glacial isostatic adjustment, relative sea level history and mantle viscosity: reconciling relative sea level model predictions for the U.S. East coast with geological constraints. Geophys. J. Int. 201, 1156–1181. <https://doi.org/10.1093/gji/ggv066>.
- Schumacher, M., King, M.A., Rougier, J., Sha, Z., Khan, S.A., Bamber, J.L., 2018. A new global GPS data set for testing and improving modelled GIA uplift rates. Geophys. J. Int. 214, 2164–2176. <https://doi.org/10.1093/gji/ggy235>.
- Sella, G.F., Stein, S., Dixon, T.H., Craymer, M., James, T.S., Mazzotti, S., Dokka, R.K., 2007. Observation of glacial isostatic adjustment in "stable" North America with GPS. Geophysical research letters. In: Shennan, I., Long, A.J., Horton, B.P. (Eds.), 2015. Handbook of sea-level Research, 34. John Wiley & Sons, Ltd, Chichester. <https://doi.org/10.1029/2006Gl027081>.
- Shennan, I., Long, A.J., Horton, B.P., 2015. Handbook of Sea-Level Research. John Wiley and Sons.
- Simon, K.M., Riva, R.E.M., Vermeersen, L.L.A., 2021. Constraint of glacial isostatic adjustment in the North Sea with geological relative sea level and GNSS vertical land motion data. Geophys. J. Int. 227, 1168–1180. <https://doi.org/10.1093/gji/ggab261>.
- Slangen, A., Katsman, C., van de Wal, R., Vermeersen, L., Riva, R., 2012. Towards regional projections of twenty-first century sea-level change based on IPCC SRES scenarios. Clim. Dyn. 38 (5–6), 1191–1209. <https://doi.org/10.1007/s00382-011-1057-6>.
- Spada, G., 2017. Glacial isostatic adjustment and contemporary sea level rise: an overview. Surv. Geophys. 38 (1), 1–33. <https://doi.org/10.1007/s10712-016-9379-x>.
- Spada, G., Melini, D., 2022. New estimates of ongoing sea level change and land movements caused by glacial isostatic adjustment in the Mediterranean region. Quat. Sci. Rev. 229, 984–998. <https://doi.org/10.1093/gji/ggab508>.
- Tarasov, L., 2013. GLAC-1b: a new data-constrained global deglacial ice sheet reconstruction from glaciological modelling and the challenge of missing ice. Geophys. Res. Abstr. 15. EGU2013-12342.
- Vacchi, M., Ghilardi, M., Stocchi, P., Furlani, S., Rossi, V., Buosi, C., Rovere, A., De Muro, S., 2020. Driving mechanisms of Holocene coastal evolution in the Bonifacio strait (Western Mediterranean). Mar. Geol. 427, 106265. <https://doi.org/10.1016/j.margeo.2020.106265>.
- Vacchi, M., Marriner, N., Morhange, C., Spada, G., Fontana, A., Rovere, A., 2016. Multiproxy assessment of Holocene relative sea-level changes in the Western Mediterranean: sea-level variability and improvements in the definition of the isostatic signal. Earth Sci. Rev. 155, 172–197. <https://doi.org/10.1016/j.earscirev.2016.02.002>.
- Wake, L., Milne, G., Leuliette, E., 2006. 20th century sea-level change along the eastern US: unravelling the contributions from steric changes, Greenland ice sheet mass balance and late Pleistocene glacial loading. Earth Planet Sci. Lett. 250, 572–580. <https://doi.org/10.1016/j.epsl.2006.08.006>.
- Whitehouse, P.L., 2018. Glacial isostatic adjustment modelling: historical perspectives, recent advances, and future directions. Earth Surf. Dyn. 6, 401–429. <https://doi.org/10.5194/esurf-6-401-2018>.
- Williams, K., Stamps, D.S., Melini, D., Spada, G., 2024. Vertical displacements and sea-level changes in eastern North America driven by glacial isostatic adjustment: An ensemble modeling approach. J. Geophys. Res. Solid Earth 129, e2023JB028250. <https://doi.org/10.1029/2023JB028250>.
- Yousefi, M., Milne, G., Li, S., Wang, K., Bartholeit, A., 2020. Constraining interseismic deformation of the Cascadia subduction zone: new insights from estimates of vertical land motion over different timescales. J. Geophys. Res. Solid Earth 125, e2019JB018248. <https://doi.org/10.1029/2019JB018248>.
- Yousefi, M., Milne, G.A., Love, R., Tarasov, L., 2018. Glacial isostatic adjustment along the Pacific Coast of central North America. Quat. Sci. Rev. 193, 288–311. <https://doi.org/10.1016/j.quascirev.2018.06.017>.